ThermoWave: A New Paradigm of Wireless Passive Temperature Monitoring via mmWave Sensing

Baicheng Chen, Huining Li, Zhengxiong Li, Xingyu Chen, Chenhan Xu, Wenyao Xu
University at Buffalo, the State University of New York, Buffalo, New York, USA
{baicheng, huiningl, zhengxio, xchen252, chenhanx, wenyaoxu @ buffalo.edu}

ABSTRACT

Temperature sensor is one of the most widespread technologies in the IoT era. Wireless temperature monitoring systems are convenient to deploy and can drive mass applications in the fields of smart home, transportation and logistics. Currently, wireless temperature monitoring products are based on microelectronic and semiconductor components, which are not cost-effective (e.g., a few dollars) and more importantly, generate electronic wastes. In this work, we present ThermoWave, a new paradigm of wireless temperature monitoring that is ecological, battery-less, and ultra-low cost. Specifically, ThermoWave is on the basis of the thermal scattering effect on millimeter-wave (mmWave) signals. Specifically, cholesteryl materials align their molecular patterns at different environmental temperatures, and this temperature-induced pattern change will be modulated and sensed by the scattered mmWave signals. There are three functional modules in the ThermoWave system. The ThermoTag is a cholesteryl material inked film or paper tag that can be conveniently attached to the object of interest to monitor temperature changes. Each ThermoTag costs less than 0.01 dollars. The temperature modulated mmWave scattering will be received by a mmWave-radar based ThermoScanner and demodulated by a software-based temperature decoder ThermoSense, which includes a model-based method (i.e., ThermoDot) for point temperature estimation and a data-driven method (i.e., ThermoNet) for thermal imaging. We prototype and evaluate the ThermoWave system performance in both controlled and real-world setups. Experimental results show that the ThermoWave achieves the precision of ±1.0°F in the range of 30°F to 120°F in a controlled setup. We also investigate the performance in real-world applications, and the ThermoWave can reach the ±3.0°F precision in the temperature estimation. We also test and discuss sustainability, durability, robustness, and cost-effectiveness of the ThermoWave in both design and experiments.

CCS CONCEPTS

• **Human-centered computing** → **Ubiquitous and mobile computing**; • **Computer systems organization** → **Embedded and cyber-physical systems**.

1 INTRODUCTION

Temperature sensors are one of the most in-demand IoT technologies to monitor physical and environmental conditions in daily-life applications. For instance, temperature-sensitive products, including most foods and medicines, are required to be in a temperature-controlled environment to maintain the best possible quality in the storage and transportation [1–4]. Due to packaging and mobility considerations, wireless temperature systems are the essential solution to monitor thermal conditions and protect package integrity and quality in practice. In the landscape of temperature monitoring system markets, the wireless temperature sensor segment grows at the highest rate—15.09 million units generated in 2019 and is expecting to reach 23.45 billion units by 2025 [5–8]. Currently, updating the existing infrastructure to support low-cost and ecological wireless temperature monitoring has been the primary trend impacting multiple industries, such as smart cities and cold chain logistics [9].

There is a set of rich literature and commercial products about wireless temperature monitoring technologies developed toward two directions (i.e., wireless temperature sensors and thermal-imaging devices). Wireless temperature sensor is often made into tags with thermal-electric temperature sensors [10–12]. Unfortunately, such technology associates with high cost, harms environment, and lacks thermal imaging capability. On the other side, thermal imaging devices read temperature distribution across space in front of the sensor [13, 14]. However, such mechanism fails to read temperature from target object with as little as a thin sheet of paper in between. Given the fact that temperature monitoring is a high demand industry that impacts every second of our daily life, a more powerful wireless temperature sensing paradigm is in urgent need for future temperature monitoring applications in scientific (e.g., material research), industrial (e.g., smart city), and medical fields (e.g., body temperature sensing).

In this study, we explore and unveil a novel material mediated wireless temperature sensing technology, using mmWave sensing. This technology aims to empower extremely low-cost (e.g., under 1 cent per sensor), flexible (e.g., soft sensor material), and ecological (e.g., environmentally friendly materials) temperature monitoring for both dot-wise and fine-grained thermal imaging results under NLOS scenario. The design rationale bases on cholesteryl material's thermal scattering effects. When the ambient temperature changes, the molecular alignment of cholesteryl material alters accordingly

B. Chen et al.
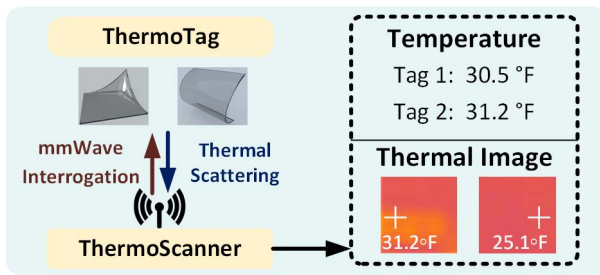
Figure 1: ThermoWave: a new ultra-low cost mmWave-scannable temperature monitoring paradigm capable of thermal imaging that utilizes flexible materials.

due to thermal expansion of inter-molecular distance, and thereby impacting scattering properties when it is probed by broad-band (e.g., 250 MHz) radio frequency (RF) signals. Motivated by such thermal scattering effect, we utilize cholesteryl materials to fabricate a film-shaped temperature tag that can change and modulate the scattered RF signals with temperature change characteristics. To exploit stronger scattering properties, we investigate the high-frequency RF signaling technologies, such as the millimeter wave (mmWave) probes, to effectively interrogate the thermal scattering effects and infer the temperature information. As shown in Fig. 1, this technology can enable a low-cost, out-of-sight, accurate temperature monitoring in environmentally restricted scenes, such as medicine storage and transportation logistics.

To this end, we present ThermoWave, a new mmWave technology based paradigm to facilitate fully passive temperature monitoring. There are three parts to the ThermoWave paradigm. (1) We first design the ThermoTag based on a thin layer of cholesteryl material stabilized on top of a thin polyvinyl chloride sheet with adhesives, which can characterize the thermal scattering effect as temperature changes. (2) We prototype a mmWave based ThermoScanner to continuously interrogate the ThermoTag and capture frequency shift of thermal scattering response in contrast to the transmitted signal. (3) The scattering response signals are input to ThermoSense, which is a software mechanism for temperature inference. For dot-wise temperature recognition, the input signals are first decomposed into a combination of wavelets via Empirical Wavelet Transform for extracting spectral features. Then, we apply a regression based ThermoDot model that utilizes extracted features in order to determine the single dot-wise temperature value. Toward thermal imaging results, we first transform the input signals into a spectrogram image using continuous-time short-time Fourier Transform. After that, the spectrogram images are fed to a customized ThermoNet (i.e., an image-to-image GAN) model for reconstructing thermal images. As a first exploration study, we use a set of metrics to evaluate ThermoWave performance (e.g., temperature inference accuracy and image structural similarity index). We evaluate the robustness of ThermoWave under different sensing distances, scanning orientations, and occlusions to show its superior performance for temperature inference. In our study, ThermoWave can measure the dot-wise temperature change from 30°F to 120°F with the precision of ±1.0°F and thermal imaging in the same temperature range with a ±3.0°F precision.

Our contribution can be summarized in three-fold:

- We investigate the thermal scattering effect that causes a temperature-related frequency shift modulation in scattered RF signals, and study the mathematical model that captures and characterizes this change with low-cost and ecological cholesteryl materials.
- We design and implement the Thermowave system, based on cholesteryl material's thermal scattering effect. First, we design a cholesteryl based ThermoTag as a temperature sensing film or sticker that attaches to an object of interest. Then, we prototype a mmWave based ThermoScanner to interrogate and receive the thermal scattering response. Finally, we develop the end-to-end software ThermoSense to extract dot-wise temperature and thermal image from the thermal scattering response.
- We evaluate ThermoWave systems performance with different configurations (e.g., ThermoTag shape and size). Moreover, we validate the robustness of ThermoWave system under different scanning distances, orientations, and occlusion conditions. We also examine the stability of ThermoWave system under a real-world scenario. System limitations are also identified and discussed.

2 BACKGROUND AND PRELIMINARIES

2.1 Thermal Scattering Effect

The crux of the proposed wireless temperature sensing paradigm is to leverage temperature-sensitive physical characteristics of specific material to retrieve temperature information via RF probing. Among existing wireless temperature sensing solutions, our method presents the benefit of extreme low-cost, flexibility, environment friendliness and advanced thermography functions. Due to cholesteryl material's temperature sensitive molecular alignment pattern [15], we select cholesteryl materials as the sensing media to convey the temperature information of target object. When cholesteryl material is attached to the target object, it will immediately reach the same temperature as the target object and keep thermal equilibrium according to the theory of thermodynamics
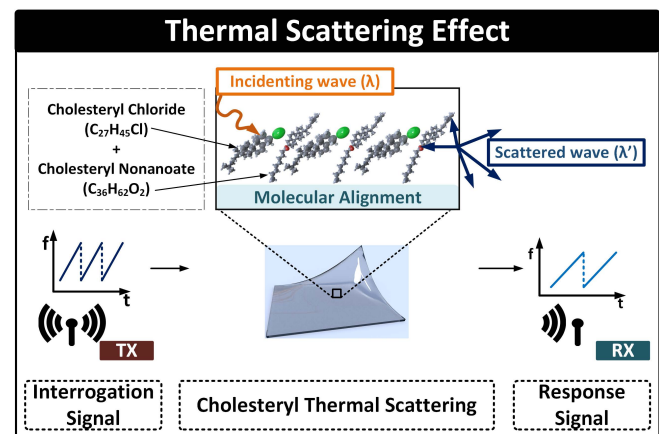
Figure 2: Cholesteryl material's temperature dependent molecular alignment directly impacts the frequency of scattering response under the illumination of mmWave.

[16]. This theory suggests that the level of average kinetic energy (i.e., temperature) of an object tends to balance with the contacting objects.When the temperature of cholesteryl material changes, its underlying structure, which contains polymersome (i.e., vessels), will alter its molecular alignment due to thermal expansion [17]. This molecular alignment directly impacts the scattering angle when such cholesteryl material is probed by broadband RF signals. Specifically, as the RF signal arrives at the location of interest, in-placed cholesteryl material scatters a response RF signal with a modulated frequency shift. The frequency shifted signal is then scattered in all directions, allowing signature capturing for temperature inference. The process of this so-called Thermal Scatter Effect is visualized in Fig. 2.

2.2 A Preliminary Study: Cholesteryl Material based mmWave Sensing

Hypothesis: Thermal scattering effect of cholesteryl material that contains unique RF scattering response from temperature caused molecular alignment can be treated as an intrinsic thermal feature. Thereby, it is possible to leverage a mmWave probe that stimulates the cholesteryl material for a frequency-shifted scattering, which contains temperature-induced modulation and contribute toward object temperature detection.

Proof-of-concept: To prove the Hypothesis, we designed and conducted a preliminary experiment using a prototype of cholesteryl material as a temperature sensing media. Specifically, our preliminary experiment is conducted in a well temperature monitored room to ensure that the environment temperature does not change while the tag changes temperature with controlled air based heating. To simulate a temperature sensing scenario, we use a table as the sensing target, and place the tag on top of the table edge to act as a temperature sensing media. Then, we place a heater on the side of the table to manually control the material temperature from 70 °F (i.e., room temperature) to 90 °F for theoretically distinct data points as we attempt to visualize the thermal scattering effect in Fig. 3. To eliminate the ground truth temperature sensor (e.g., digital thermometer) from interfering with the interrogation signal from mmWave probe or response signal from tag, we adopt an infrared camera that can read tag temperature while placed behind the mmWave probe. To illuminate the cholesteryl material, we utilize a 24GHz frequency modulated continuous wave (FMCW) radar with a 250MHz bandwidth. After obtaining the thermal scattering response from the material, we analyze the signal utilizing the spectral plot that presents a direct connection between temperature difference and frequency shift of scattered signal. As shown in Fig. 3, the thermal scattering responses of cholesteryl material at $70°Fvs.90°F$ are uniquely different. This proves that cholesteryl material can be used to perform temperature monitoring, which further verifies the feasibility and effectiveness of obtaining temperature value via material mediated temperature sensing.

3 THERMOWAVE OVERVIEW

The ThermoWave paradigm comprises three main modules: ThermoTag, ThermoScanner, and ThermoSense to realize material-mediated wireless temperature sensing (see the illustration in Fig. 4).
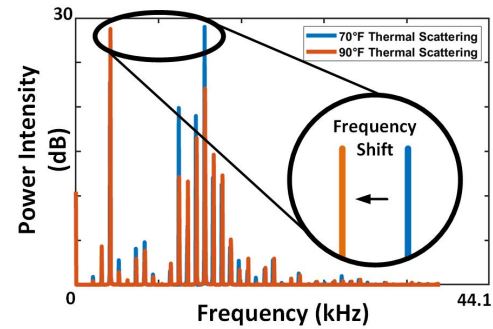
Figure 3: Thermal scattering responses from cholesteryl material show evident frequency shift in spectrum analysis. Compared to response at 70 °F, the frequency shifted response at 90 °F have a tone that is few kHz lower.

ThermoTag: ThermoTag is a Cholesteryl material based passive wireless temperature sensor that attaches to the surface of target object for wireless temperature sensing. As target object's surface temperature changes, ThermoTag's temperature will instantly follow and alter its cholesteryl molecular alignment accordingly. As ThermoTag's molecular alignment changes, its mmWave scattering properties will also change as shown in Fig. 3. The resulting mmWave scattering properties can be captured by the customized ThermoScanner for temperature inference.

ThermoScanner: Considering the prospect of mmWave with a 5G technology in wireless communication as well as its large bandwidth opportunities, we prototype a tag scanner based on 24Ghz FMCW radar, namely ThermoScanner. It is worth to mention that the cost for a mmWave radar sensor is below $24 and a mmWave radar modality is below $50, which is projected to keep decreasing along with infrastructural deployment [18, 19]. To localize the ThermoTag, the ThermoScanner employs a pair of four by four antenna arrays with antenna directivity of 19.8 dBi to enhance the precision. While the ThermoScanner continuously interrogates ThermoTag, the thermal scattering response is recorded continuously for temperature inference. Without further adieu, ThermoScanner sends recorded signal to ThermoSense for both dot-wise temperature inference and thermal imaging.

ThermoSense: ThermoSense is a software mechanism to facilitate both dot-wise temperature recognition and thermal image inference. However, results from dot-wise temperature recognition is a single value while a thermal image is multi-dimensional. Thus, we allocate two models to perform the two specific temperature inference tasks. For dot-wise temperature recognition, we first convert the scattering signals from time domain to frequency domain via Empirical Wavelet Transform, then, a feature extractor is developed to reduce data dimension to an array of 38 features from each pre-processed signal, after that, we use a regressor based **ThermoDot** model to map the feature array to a specific temperature value. In order to achieve thermal imaging, we first transform thermal scattering response into spectrogram image using continuous-time short-time Fourier Transform. Then, we develop a **ThermoNet** model based on generative adversarial network (GAN) to reconstruct thermal images from spectrogram input data.
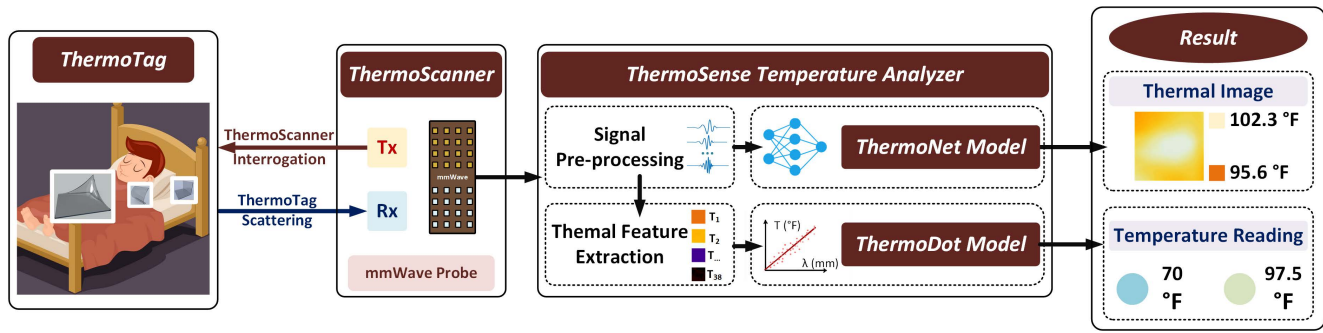
Figure 4: We present the ThermoWave paradigm with its three core modules (i.e., ThermoTag,ThermoScanner,and ThermoSense). ThermoTag can be placed on be wrist for skin temperature, bed for ambient temperature, and bed sheet for body thermal imaging. ThermoScanner continuously interrogates ThermoTag to capture temperature cased thermal scattering response, then, the response signals are sent to ThermoDot model and ThermoNet model to obtain dot-wise temperature reading and thermal imaging, respectively.

4 THERMOTAG DESIGN

4.1 ThermoTag Implementation

In order to sustain temperature sensing capability, ThermoTag is manufactured from cholesteryl materials (e.g., cholesteryl benzoate) that can withstand temperature up to 149 °C (i.e., 300 °F) without being damaged [20, 21]. This facilitates a wide range of applications , such as high temperature chamber monitoring, boiling liquid sensing, and heating radiator monitoring. During the manufacturing process, we stabilize a thin layer of cholesteryl material on top of a thin substrate layer of polyvinyl chloride sheet with adhesives, which enables high elasticity [22] of ThermoTag. As a result, ThermoTag can be manually suppressed to various shapes (e.g., bend, camber, curve, fold, wrap) without permanent deformation as shown in Fig. 5. In this way, it is flexible to deploy ThermoTag in many complicated scenarios, such as high voltage electric cable temperature monitoring within a power cage over the length of the cord, cold chain transportation with non-rigid medicine containers, and vehicle tire temperature monitoring while inflated [23–25]. It is worth to mention that ThermoTag is very lost-cost. In contrast to commodity RFID temperature tags with a price of 1.99 dollars in a bulk order, one functional slice of ThermoTag (1cm x 1cm square shaped film) costs less than one US cent which is a significant reduction [26, 27].
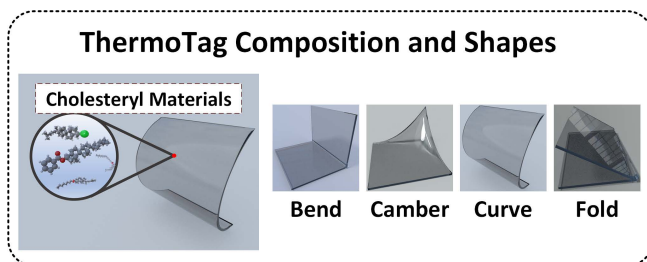

Figure 5: ThermoTag utilizes soft cholesteryl material that can be manufactured and stressed into various shapes for complex deployment scenarios.

4.2 ThermoTag Modeling

The temperature variation of Cholesteryl material based ThermoTag can disturb its thermal scattering of mmWave signals. In this subsection, we establish a physical model to illustrate the thermal scattering effect of ThermoTag.

ThermoTag is designated to be a temperature sensing media that attaches to a target surface. When the target's temperature changes, ThermoTag's temperature inevitably follows. As the temperature of cholesteryl material-based ThermoTag varies, its inner molecular alignment (i.e., three-dimensional geometry shown in Fig. 2) will alter due to the Flory−Huggins parameter χ [28], expressed as:

$$\chi(T) = \frac{v_0}{kT}(\delta_1 - \delta_2)^2, \tag{1}$$

where T is temperature, and $\chi(T)$ is the Flory−Huggins parameter as a function of temperature, v_0 is volume of the cholesteryl mixture, δ_1 and δ_2 are the solubility constants for the cholesteryl material polymers in the mixture, k is the real gas constant. The above presents a crucial monotonous relationship between the temperature of ThermoTag and the Flory−Huggins parameter of the material, which generalizes the underlying molecular alignment pattern, This facilitates further interpretation of temperature through the physical trait using wireless means.

When the interrogation mmWave signal reaches ThermoTag (i.e., cholesteryl material mixture), the tag will generate a frequency-shifted scattering based on temperature as shown in Fig. 4. The temperature induced frequency shift relationship is formulated in Eq. (2):

$$\lambda_r(\lambda_i, T) = \lambda_i cos \frac{1}{2}\left[\left(sin^{-1}\left(\frac{l}{l'}sin(\Phi_i)\right) + sin^{-1}\left(\frac{l}{l'}sin(\Phi_r(\chi(T)))\right)\right], \tag{2}$$

where l is the index of refraction of the environment (e.g., air), and l' is the index of refraction of cholesteryl mixture. Assuming the relative location and orientation between the ThermoTag and ThermoScanner does not change during the period of sensing, Φ_i being the angle of entrance for the incident wave, can be replaced with a constant. Φ_r is the angle of exit for the return wave as function of the temperature dependent Flory-Huggins parameter χ which bases on temperature T. Upon removing potential constant

values, a lean model is derived in Eq. (3),

$$\lambda_r(\lambda_i, T) = \lambda_i cos[\Phi_r(\chi(T))], \tag{3}$$

where T is the temperature, λ_i is the frequency of the incident wave, and $\lambda_r(\lambda_i, T)$ is the frequency of the response wave [15, 17]. It is noteworthy that thermal scattering emits frequency modulated response signal at all directions, allowing flexible deployment of ThermoTag in various scenarios.

To summarize, ThermoTag's underlying molecular alignment is changed by the variation of temperature, such alignment variation further affects thermal scattering properties for mmWave.

4.3 ThermoTag Ecology Analysis

ThermoTag is an organic tag based on cholesteryl materials which is biodegradable [29]. ThermoTag is also highly reusable due to the relatively low melting point and can be used to forge a new tag with different shapes without losing significant volume. ThermoTag's ecological life cycle begins with cholesteryl materials being mixed by heating the solid mixture into liquid, the liquid is then poured to mold for shaping. During the molding and shaping stage, it is important that the mixture is kept at a high temperature (around 300 °F) which allows the liquid to keep flowing and change shape. The resulting tag can be reused immediately after cooling. Any residue without contamination can be collected and melted for another reuse cycle. Therefore, ThermoTag allows the reuse and safe disposal of cholesteryl material and is an ecological sensor.

5 THERMODOT SENSING SCHEME

5.1 Thermal Scattering Response Acquisition

ThermoTag scatters frequency-shifted response signal with modulated temperature information as the intrinsic property, it is important to ensure that ThermoScanner receives and parses different frequency shifts that occur at different temperatures. Most of mmWave radars support both pulse and continuous wave modes. sampling rate compare to the pulse mode. High amplitude pulse waves can undermine the thermal scattering effect in return, making temperature prediction difficult. The continuous wave mode allows continuous reception of thermal scattering from ThermoTag, which enables a higher sampling rate. Therefore, the ThermoWave design selects the continuous wave mode with a frequency modulated continuous wave (FMCW) radar. When ThermoScanner emits the interrogation signal from TX terminal to illuminate ThermoTag, ThermoTag undergoes the thermal scattering effect. This allows ThermoScanner RX terminal to receive the response with intrinsic thermal scattering effects. It is worth to mention that such sensing mechanism is not restricted by the orientation setup as the scattering of ThermoTag's modulated response signal occurs at all directions. Finally, the thermal scattering response encapsulating temperature characteristics is acquired and passed to the ThermoSense module.

5.2 Scattered Signal Transformation

To perform the effective temperature estimation, there are critical pre-processing and transformation operations (i.e., filtered, decomposed) to facilitate an accurate frequency shift analysis. Since the
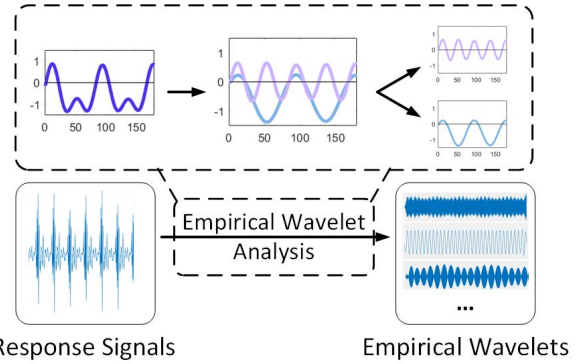

Figure 6: Empirical wavelet analysis transforms acquired signal into a series of wavelets for frequency analysis.

frequency shift characteristic is crucial in thermal scattering response yet highly complex (i.e., variance in thermal scattering response's amplitude and frequency is non-memorizable due to large bandwidth), we propose to utilize a signal decomposition technique that separate thermal scattering signals into a set of wavelets to allow effective and efficient amplitude-frequency spectral analysis. Thus, we utilize Empirical Wavelet Transform (EWT) [30] to perform frequency domain analysis by detecting local maximas in the wavelet spectrum in our application.

To formulate EWT, we show the reconstruction of the ThermoTag response signal that is separated into a series of wavelets by EWT, whose sum infinitely-approaches the original thermal scattering response:

$$f(t) = W_f^\epsilon(0, t) \star \phi_1(t) + \sum_{n=1}^{N} W_f^\epsilon(n, t) \star \psi_n(t), \tag{4}$$

$$f(t) = (W_f^\epsilon(\overset{\wedge}{0}, \omega)(\overset{\wedge}{\phi}_1(\omega) + \sum_{n=1}^{N}(W_f^\epsilon(\hat{n}, \omega)(\overset{\wedge}{\psi}_n(\omega))^\vee, \tag{5}$$

where $f(t)$ is the synthesized signal that infinitely approaches original ThermoTag's thermal scattering response, t is time, ω is wavelength, which is inversely proportional to frequency, $\phi_n(\omega)$ is the empirical scaling function, $\psi_n(\omega)$ is the empirical wavelets, N is the number of wavelets in total. $W_f^\epsilon(0, t)$ is the approximation coefficients and $W_f^\epsilon(n, t)$ is the detail coefficients given by the inner products with the empirical wavelets. Eq. (5) is the representation of Eq. (4) wavelet reconstruction in terms of fourier transform that displays frequency-domain wavelet summation. To this end, the signal is decomposed into a series of empirical wavelets as shown in Fig. 6 for feature extraction.

Table 1: Feature List in the ThermoDot model

Types	Features
Spectral	Crest Factor [31], RMS Amplitude, Flatness [32], Skewness [33], Kurtosis [34], PNCC-20, MFCC-5
Temporal	Lowest Value, 50th percentile, Mean Value, 75th percentile, Highest Value, Standard Deviation, Kurtosis, Skewness

5.3 Feature Extraction

Thermal scattering response is characterized by the frequency shift alone with amplitude variations, making simple model-driven approaches quickly fail due to the complexity of spectral data in a bandwidth of 250MHz. Thus, we implement feature extraction from the wavelets that can accurately and effectively describe the frequency-shifted signals without concern from noisy signal impacting sensing accuracy. To comprehend the thermal scattering response, we enlist features in two types, i.e., spectral and temporal features. It is noteworthy that we employ spectral analysis that takes the signal to filter, then analyze the distribution of signal intensity. For instance, mel-frequency cepstral coefficients (MFCC) [35–38] and power-normalized cepstral coefficients (PNCC) [39–41] are exceptional power-frequency distribution analyzers that provide detailed comprehension of the frequency shift and is capable of reducing noise impacts in the later prediction. Notably, PNCC are scalar coefficients based on gammatone channel filtering. The channel bias minimization is used to suppress the noise effects as shown in Eqs. (6) and (7) [42]:

$$V[f, c] = (\frac{kP[f, c]\widetilde{S}[f, c]}{\mu[f]})^{1/15}, \qquad (6)$$

where $V[f, c]$ is the power function non-linearity, f and c are the frame and channel indices, respectively. k is the DFT size, empirically determined to be 1024. $P[f, c]$ is the result of signal after Preemphasis, Short-Time Fourier Transform, Magnitude Squared, and Gammatone Frequency Integration. $\widetilde{S}[f, c]$ is the result of $P[f, c]$ after medium-time power calculation, asymmetric noise suppression with temporal masking, and weight smoothing. $\mu[f]$ is the mean power estimate of frame f formulated in Eq. (7):

$$\mu[f] = \lambda_\mu \mu[f - 1] + \frac{(1 - \lambda_\mu)}{C} \sum_{C-1}^{c=0} T[f, c], \qquad (7)$$

where C represents the total number of frequency channels. λ_μ is empirically determined to be 0.999 as the forgetting factor. $T[f, c]$ is the the result of $\widetilde{S}[f, c]$ after time-frequency normalization by elementary multiplication of $P[f, c]$ and $\widetilde{S}[f, c]$. The initial value of $\mu[f]$, $\mu[0]$, is determined to be 16161 dB/Hz based on mean power of signals using data set in our preliminary study.

The power function non-linearity then goes through a discrete cosine transform. The resulting matrix is converted into a one-dimensional array to reduce the feature count for a better efficiency, i.e., generating 20 coefficients from 20 Gammatone channels, respectively. The origin of PNCC work includes the operation of mean normalization, considering that the feature coefficients are used for the regression analyzes. Note that mean normalization is opted out because this operation will not provide further benefits in thermal analysis. Up to this point, scalar coefficients are effectively collected for regression. The complete feature list categorized into two types(i.e., Spectral, Temporal) is shown in Table 1.

5.4 ThermoDot Regression Model

The feature array of 38 scalar values are extracted from each segment of RF signals, and we feed the feature arrays with one temperature label (i.e., the ground truth) into a regression model to solve the prediction modeling problem as shown in Algorithm 1. We start

---

Algorithm 1 ThermoDot Algorithm

Input: S: mmWave signal
  L: Signal segment count
  K: Feature count
  M: Trained regression model
  ε: Number of trees
Output: T: Point Temperature Prediction Results

```
 1: T = [   ];
 2: M = loadModel();                    ▷ Load trained model
 3: S_w = EWT(S);                       ▷ Apply wavelet transform
 4: for i = 1, 2, ..., L do
 5:     ϱ = S_w(i);                     ▷ Acquire signal segment
 6:     features = [   ];               ▷ Initialize feature array
 7:     for j = 1, 2, ..., K do
 8:         ϑ = featureFunction_j(ϱ);   ▷ Acquire Feature
 9:         features.append(ϑ);
10:     end for
11:     t = M.Regression(features, ε);  ▷ Predict
12:     T.append(t);
13: end for
14: Return T.                          ▷ return results
```

with choosing a meta-algorithm to perform the task. There are two major advantages for employing the bootstrap aggregation (bagging) method [43]. 1) Ensemble learning allows multiple regressors to generate independent prediction result and aggregate them into final decision with better confidence. Weighting is given by the accuracy of each independent regressor to boost the accuracy of final decision, enabling higher accuracy. 2) Bagging allows low variance value that makes output more stable in temperature prediction, which prevents overfitting. The series of feature arrays is fed into bagging model that utilizes the ThermoDot model in Algorithm 1 to perform the regression prediction and return temperature estimation corresponding to the feature arrays. After feeding the bagging regressor with a list of feature vectors as input and a list of temperature values as the ground truth, the regressor solves for the discrete parameters to fit training data. The resulting ThermoDot model will then take in thermal scattering response and return a single value temperature output as shown in Fig. 7.
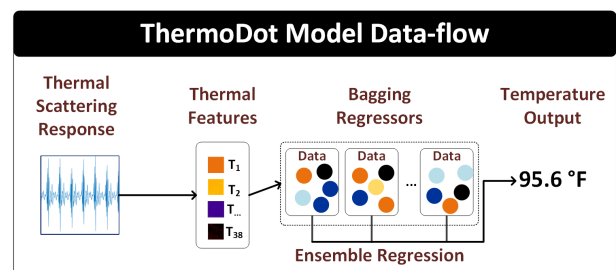

Figure 7: ThermoDot model data flow from thermal scattering response to exact temperature value.
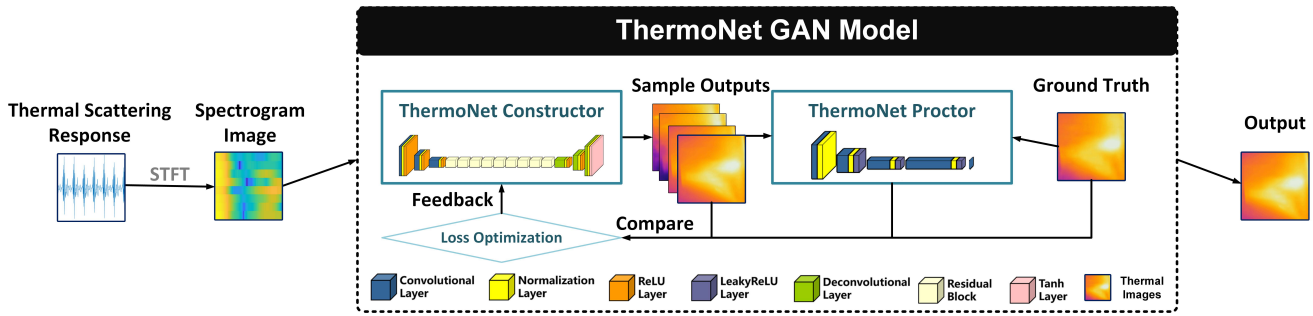
Figure 8: ThermoNet leverages spectrogram image from thermal scattering response and its corresponding ground truth thermal image to train the image-to-image neural network model, the resulting model has the capability to generate thermal images from spectrogram images. The ThermoNet Constructor keeps generating sample outputs based on spectrogram image while the ThermoNet Proctor decides whether the sample output is close enough to the ground truth. When the ThermoNet Proctor denies the sample output, the results are compared and sent to Loss Optimization for ThermoNet Constructor to generate better (i.e., more accurate) output in the future.

6 THERMONET SENSING SCHEME

6.1 Thermal Scattering Response to Spectrogram Transformation

The objective of thermal imaging is the retrieval of surface temperature in the form of a thermal image from thermal scattering response. To realize it, the first step is to transform thermal scattering response signal from one dimensional spectral-temporal function, into a two dimensional spectral-image function. Based on the advantage that continuous-time short-time Fourier Transform (STFT) is more applicable for real-time processing compare to two dimensional wavelet transform's high computation overload, we adopt STFT [44] for transforming the spectrogram signal into a three dimensional representation, formulated as Eq. (8):

$$STFT\{x(t)\}(\tau, \Omega) = \int_{-\infty}^{\infty} x(t)\Omega(t - \tau)e^{-j\lambda t}dt, \qquad (8)$$

where $\Omega(\tau)$ is the Gaussian window function, $x(t)$ is the signal to be transformed, λ is the frequency and $STFT\{x(t)\}(\tau, \Omega)$ is the resulting spectrogram image that captures essence of thermal scattering response. The result is a three dimensional data, we map one of the dimension to color space in order to generate a temperature image. At this point, the problem is reduced to mapping a spectrogram image to a correct thermal image.

6.2 ThermoNet Model Construction

In order to solve the spectrogram image to thermal imaging mapping problem, pixels in spectrogram image must be mapped to pixels in thermal image. Such mapping must not only capture the general color to color relationship, but the image structure, which encapsulates the temperature distribution over the thermal image. However, a typical thermal image have over 65,536 pixels (256x256), which can lead to four billion links to a 65,536 pixel spectrogram image, making it nearly impossible to compute over short period of time in temperature sensing applications. Thus, we implement a neural network to solve the image to image mapping problem. We employ the Pix2pix model [45], which is a Generative Adversarial Network

(GAN) [46] model specifically designed for image-to-image transformation tasks. Different from Convolutional Neural Network (CNN)'s dependency on a fixed loss function to optimize the neural network, GAN implements an adaptive loss function, this allows GAN to solve problem of neural network generation without a cumbersome loss function design. We formulate the ThermoNet model as follows:

$$\min_G \max_D V(D, G) = E_{\zeta \sim p_{data}(\zeta)}[logD(\zeta)]$$
$$+ E_{z \sim p_z(z)}[log(1 - D(G(z)))], \qquad (9)$$

$$\max_D V(D) = E_{\zeta \sim p_{data}(\zeta)}[logD(\zeta)]$$
$$+ E_{z \sim p_z(z)}[log(1 - D(G(z)))], \qquad (10)$$

$$\min_G V(G) = E_{z \sim p_z(z)}[log(1 - D(G(z)))], \qquad (11)$$

where G is the generator (i.e., constructor) function, D is the discriminator (i.e., proctor) function, z is the input data being our image from spectrogram transform, and ζ is the training data being temperature image from IR camera. To achieve ideal transformation result, *ThermoNet* requires a Constructor and a Proctor to collaborate and compete against each other.

(a) Constructor is a network of "encoder-decoder" structure. The encoder has a three-layer convolution structure with a first layer depth of 64, the second layer depth of 128, and the third layer depth of 256. Each layer is followed by a ReLU activation function. In order to abstract and retain more information, we add more weighted layers between the encoder and the decoder. We use 9 residual blocks because the residual blocks contain skip connections which can concatenates all channels between layers. To capture the details in image, the decoder is designed with three layers of deconvolution layers that upsamples the image by eight times larger, magnifying small differences in image.

(b) Proctor is a network of "encoder" structure that contains four layers of convolution. The other three convolutions use LeakyReLU, except that the first layer uses the ReLU activation function [47]. The proctor is capable of determining whether the image from constructor is similar enough compared to the ground truth. The
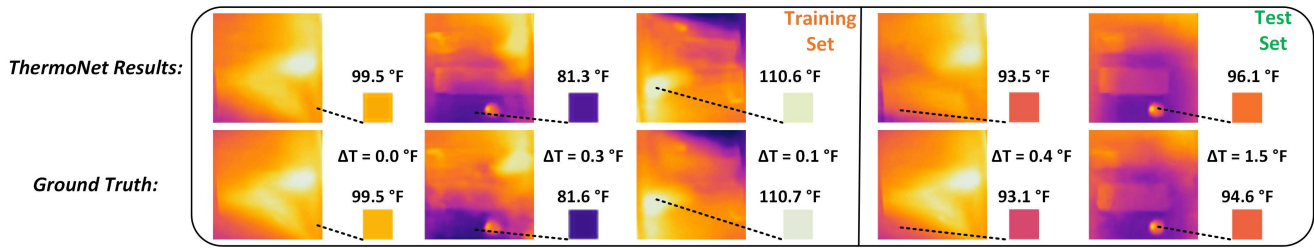
Figure 9: Comparison between thermal images generated by ThermoNet and ground truth. ThermoNet is capable of capturing the details on thermal image and regenerating them in prediction, making target detection possible using edge detection. With a large amount of training samples, ThermoNet meets the expectation of generating thermal images in untrained (test set) scenarios that are also extremely close to the ground truth in terms of both image structure, and image detail.

binary decision generated by proctor is then send to optimizer that allows the constructor to generate better results.

The workflow is shown in Fig. 8, as the constructor produces batches of thermal images as sample output, the proctor determines if the generated thermal image outputs are close enough to the ground truth thermal image. The output thermal images from proctor and the losses were sent to the optimizer, then, the optimizer enhances the weights in the constructor. At the end, the trained ThermoNet model is able to produce temperature images given the input of spectrogram image without the exact temperature image in training database as shown in Fig. 9.

7 EVALUATION SETUP

7.1 Experimental preparation

To evaluate the system, we conduct controlled experiments in a lab condition. The experiment setup is shown in Fig. 10. We fabricate the ThermoTag using a square thin film with the side length of 15 cm and the thickness of approximately 0.01 cm. The ThermoTag is attached to the inner wall of the cabinet while ThermoScanner is placed outside the cabinet. We then align the ThermoScanner to the direction of the ThermoTag starting from a distance of 25 cm. Note that there is no physical blockage between ThermoTag and ThermoScanner except the wall of cabinet box in the overall performance study.Room air temperature is hold constant at 70 °F to eliminate variation in heat dissipation across different evaluation experiments. To collect ground truth , we utilize a wired thermometer with precision of $\pm 1.0°F$ and an IR camera with precision of
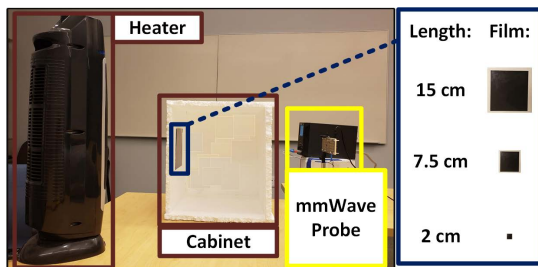
Figure 10: The film shaped ThermoTag is attached to the left wall inside the cubic foam cabinet, ThermoScanner is placed on the outer of right wall of the cabinet. The heater heats up the air in the cabinet, and thus heating up ThermoTag.

$\pm 3.0°F$ to compare with results from ThermoDot and ThermoNet, respectively [48, 49]. We evaluate the system performance under the temperature ranging from 30°F to 120 °F for all experiments, that can satisfy various scenarios such as room temperature monitoring, and food/medicine package temperature monitoring.

Application Protocol: To make ThermoWave easily deployable, the system employs a ready to sense protocol that automatically performs a scan for ThermoTags in the environment. After a ThermoTag is localized, ThermoScanner will continuously interrogate the tag for thermal scattering response, and perform temperature inference using ThermoDot and ThermoNet.

Data Collection and Preparation: Due to ThermoWave's paradigm containing two modules with unique output, two separate groups of ground truth data is collected for ThermoDot and ThermoNet. Utilizing the digital thermometer, a camera is placed to record the continuous temperature change of ThermoTag and the temperature values are obtained using optical character recognition. As a result of high-speed continuous data collection from ThermoScanner, 90,000 lines of feature array is collected and a 75%-25% split is utilized to separate the training and testing data. For the IR camera, its seven frame per second video frame rate forced ThermoNet's sampling rate to seven Hz with alignment. ThermoNet is a data-intensive model, we collected 105,790 thermal images and generated the same number of spectrogram image for ThermoNet model training and testing. To effectively assess the performance of the two models, we collect a single group of data for training, and test it against different scenarios that were not trained.

7.2 Performance Metrics

To analyze the ThermoWave performance in both dot-wise sensing and thermal imaging, we introduce performance metrics tailoring to ThermoDot and ThermoNet's output data format.

7.2.1 ThermoDot Metrics. In order to assess ThermoDot's ability to correctly derive single temperature value from a specific location using mmWave signal, we prepared three numerical metrics to evaluate the performance of dot temperature sensing, including percentage accuracy, maximum error, and correlation coefficient.

Percentage accuracy: Correct temperature prediction is defined as value predicted within the precision tolerance (i.e., threshold) of ground truth value.

Maximum error: Average of the top 1% error between predicted value and ground truth value.

Correlation coefficient: To have a general grasp on how close is the predicted temperature value to ground truth temperature value, correlation coefficient is employed [50]. Higher value (with maximum value of 1) indicate better routine system performance.

7.2.2 ThermoNet Metrics. The metrics for ThermoNet need to consider the two-dimension characteristics of the output and ground truth. Since thermal imaging is commonly done by IR systems as a two dimensional image reading with each pixel containing RGB components, we used the IR imaging system FLIR ONE PRO with approximately ± 3.0 °F precision as our ground truth. To evaluate the thermal imaging performance in both macro and micro level, we utilize a total of three metrics that can effectively compare the similarity between two images.

Structural Similarity Index: We utilize Structural Similarity Index (SSIM) [51, 52] for the thermal image structural comparison between prediction and ground truth. SSIM is based on three measures of two thermal images, i.e., luminance, contrast, and structure, which correlates to intensity, distribution, and target location in thermal image. The SSIM we used is formulated as:

$$SSIM(p, g) = [l(p, g)] * [c(p, g)] * [s(p, g)], \quad (12)$$

where p and g are the predicted thermal image and ground truth thermal image, respectively. When the value of $SSIM\ (p, g)$ reaches 1, p and g shares the highest similarity, which means the predicted thermal image is nearly identical to the ground truth. $l(p, g), c(p, g)$, and $s(p, g)$ are the individual measure of the similarity in luminance, contrast, and structure, respectively.

Peak Signal to Noise Ratio: We use a MSE based peak signal to noise ratio (PSNR) to verify the estimated thermal image quality as calculated below:

$$MSE = \frac{\sum_{a=1,b=1}^{A,B} [I_1(a, b) - I_2(a, b)]^2}{A * B}, \quad (13)$$

where a and b are indices of 2-D image under the thermal image resolution (A,B) pixels in horizontal and vertical axis, respectively. I_1 is the ground truth, and I_2 is the generated thermal image. Based on MSE, the PSNR is formulated as:

$$PSNR = 10 \log_{10} \frac{R^2}{MSE}, \quad (14)$$

where R is the maximum value of each pixel value in I_1 and I_2 (i.e., R is 255 if I_1 and I_2 is read as uint8 format and R is 1 if I_1 and I_2 is read as floating point format).

Percentage Accuracy: Percentage accuracy is calculated via counting the number of pixels in generated thermal image (I) that are within Δ distance from ground truth thermal image (T) and divding by the total number of pixels in thermal image. Percentage Accuracy can be expressed as:

$$Accuracy = \frac{count(|I - T| < \Delta)}{count(I)} * 100\%, \quad (15)$$

8 THERMOWAVE EVALUATION

8.1 Overall Performance

We evaluate the temperature inference accuracy from multiple aspects for both dot-wise temperature sensing and thermal imaging.
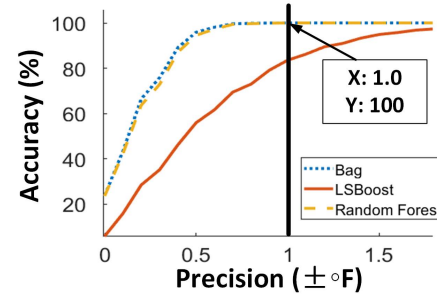
Figure 11: Micro-benchmark of temperature recognition accuracy versus precision tolerance comparing three typical regressor algorithm.

Dot-wise Performance. ThermoDot shows reliable performance in dot-wise temperature sensing in by accurately reading the temperature values of ThermoTag. As shown in Fig. 11, the bag algorithm shows the best performance compare to LSBoost and Random Forest. By comparing the prediction results of ThermoDot to the ground truth temperature values, the correlation coefficient is determined to be 0.99993. This means that ThermoDot's prediction result is extremely close to the actual temperature value if not exactly the same. With the maximum error being ±0.97 °F, ThermoDot's precision in temperature inference can be determined to be ±1.0 °F, which is exactly the same as the ground truth temperature measuring device. In another word, ThermoDot's exceptional temperature inference performance is not over-fitted, and arguably bottle-necked by the ground truth sensing device. For percentage accuracy, ThermoDot is capable of returning 99.9% of temperature readings under the precision of ±1.0 °F. For all subsequent evaluations, the highest accuracy possible would be the 100% with the standard precision of ±1.0 °F.

Thermal Imaging Performance. ThermoWave system relies on ThermoNet module to produce thermal images, and the temperature image can be analyzed in two-fold. First, in a two-dimensional temperature matrix perspective, each pixel is changed to temperature based on color, ThermoWave achieves an overall accuracy of 99.16% under precision of ±3.0°F across the two-dimensional sensing range with MSE is calculated to be 2.2351. At around 85 °F, the temperature imaging device has an precision of approximately ±5°F, which states that given a more accurate ground truth device, ThermoNet's performance in per pixel temperature accuracy can be higher than the IR imaging device. On the other hand, the two-dimensional data is viewed as a stand-alone image, PSNR is calculated based on the prediction result from ThermoNet to ground truth IR image. Examples of the image to image comparison is shown in Fig. 9. PSNR is determined to be 23.9872 for the collection of the standard data set. The SSIM from generated temperature image to ground truth temperature image is determined to be 0.9439, with SSIM being close to 1, meaning the generated image and ground truth image is very close, ThermoWave proves to be an accurate system.

8.2 Performance of Different Configurations

When ThermoWave system is applied in different scenarios, it is common that parameters such as sensing distance will vary from

experiment condition. We evaluate ThermoWave system with different parameter variation to assess the reliability.

ThermoTag Shape. When ThermoTag is shaped to conform with the sensing target's surface, the shape alone might have an impact in the temperature recognition. Thus, we test ThermoTag in irregular shapes such as bend, camber, curve, and fold to simulate various conditions such as sensor taped to the wall, fixed into corners, and tied to cables. The result shows ThermoWave system remains in high performance with dot-wise temperature inference score averaging to 99.9 % accuracy, ± 1.4522 °F max error, and 0.9993 correlation coefficient. ThermoNet scores average to 23.5174 PSNR and 0.9407 SSIM. In conclusion, ThermoWave is able to retain 99% accuracy at all four tag shapes for both dot-wise temperature sensing and thermal imaging. The performance is shown in Fig. 12, results have proven that ThermoWave system is fully functional with different tag shapes.
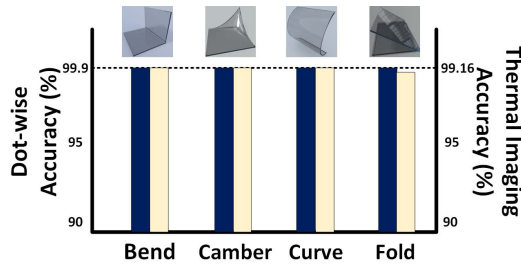

Figure 12: Performance for both dot-wise temperature and thermal imaging under different ThermoTag shapes.

ThermoTag Size. A crucial parameter of the sensor is its physical size (i.e., surface area in thin-film format), which directly contributes to the occurrence rate of thermal scattering effect. Thus, it is necessary to examine the impact of ThermoTag size to ThermoWave system performance. We used three sizes of square-shaped sensors with length 15 cm, 7.5 cm, and 2 cm as shown in Fig. 10. Performance scores are shown in Table 2 and 3 for dot-wise temperature sensing and thermal imaging, respectively. It is also noteworthy that the distance capacity of ThermoTag in relation to the size is expected to exhibit positive correlation. Our intuition is to use radar

Table 2: Dot-wise evaluation performance of different ThermoTag sizes.

Sensor length	% Accuracy	Maximum error (° F)
2 cm	**99.8**	1.5
7.5 cm	**99.9**	1.2
15 cm	**99.9**	1.0

Table 3: Thermal imaging evaluation performance of different ThermoTag sizes

Sensor length	% Accuracy	PSNR	**SSIM**
2 cm	97.7	21.1184	**0.9435**
7.5 cm	99.1	23.5449	**0.9436**
15 cm	99.2	23.9872	**0.9439**

cross section (RCS) to estimate the distance capacity in free space. However, thermal scattering effect is different from the material's reflection property, making RCS an inaccurate description. Thus, we empirically determine the distance capacity of a ThermoTag with 2 cm side length to be 50 cm. The overall high sensing accuracy result proves ThermoWave system is highly reliable with different sensor sizes for various application scenarios.

9 ROBUSTNESS ANALYSIS

9.1 Impact of Occlusion

One critical feature of ThermoWave system is passive wireless and functions in NLOS scenarios. Thus, we chose four universal occlusion scenarios in such packaging material occlusion, the thickness for bubble bag, foam, paper, wood subjects are 1.0 cm, 1.0 cm, 0.01 cm, 6.35 cm, and 2.54 cm, respectively. Among the thermal imaging assessments, ThermoWave system keeps PSNR above 22.5 and 0.95 SSIM for all four occlusions as shown in Fig. 13, proving its usability. Without surprise, IR camera's result showed thermal image for the blocking object instead of ThermoTag during the heating and cooling period, which stayed the same throughout the experiment session. This result shows ThermoWave's crucial advantage over existing IR cameras that utilizes mmWave as media to communicate with ThermoTag that achieves thermal imaging in NLOS scenarios.
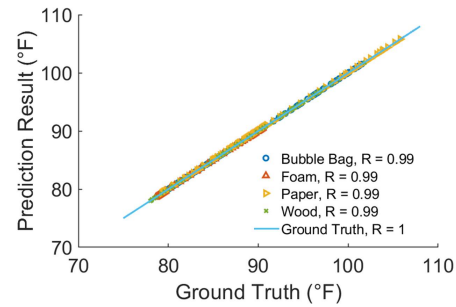

Figure 13: Dot-wise Performance under occlusion.

9.2 Impact of Sensing Distance

To validate ThermoWave's usability in contact-less (i.e., zero to ten cm) and wireless (above 50 cm) application scenarios, we performed a series of experiments with sensing distance ranging from 0.25 m to 2 m. Results have shown minimum accuracy change (i.e., above 99%) as the ThermoTag with side length 15cm moved up to two meters. Based on sensing capacity of mmWave, ThermoWave system is expected to perform high accurate temperature sensing with further distance than two meters. Thus, ThermoWave is capable and suitable for many industrial applications such as cold chain transportation in logistics.

9.3 Impact of Scanning orientation

The impact of sensing angle is a common concern when testing wireless communication, and it is important to have a device that works with various sensing angles to be robust. Therefore, we measure the dot-wise performance of ThermoWave by having a ThermoTag fixed on top of sensing target, and ThermoScanner

to move around the sensing target for angular adjustments. Due to the fact that the film shaped ThermoTag is symmetrical on all axis, we measure angles from 0 degrees to 90 degrees with 15 degrees of increment. Based on performance results shown in Fig. 14, the percentage accuracy was in the high 90s from 45 to 90 degrees with correlation coefficient averaging to 0.9985, proving ThermoWave is strong with different sensing angles for various sensing applications.
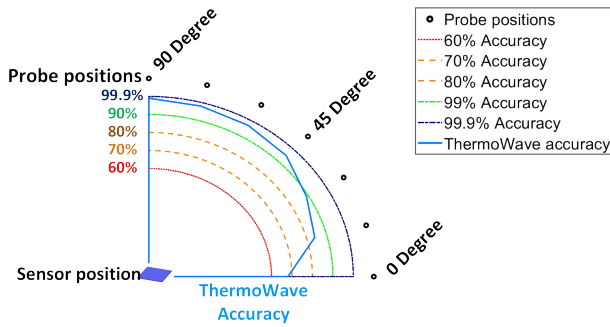

Figure 14: ThermoDot performance under different scanning orientations with ThermoTag fixed in location and ThermoScanner rotating around.

9.4 Impact of Sampling Rate

It is very worthy to mention the importance of the time that ThermoWave takes to acquire signal, which is directly proportional to the temporal efficiency in applications. Thus, we assess ThermoWave's performance under various sampling rates for both dot-wise and thermal imaging models. While the wired thermometer can give continuous readings for ThermoDot ground truth, the IR camera has a limitation of around seven frames per second, limiting the sampling rate for ThermoNet's ground truth. Thereby, we examine ThermoWave's sampling rate from one Hz to seven Hz. Results show that ThermoWave can achieve seven Hz sampling rate without significant loss of accuracy, as shown in Fig. 15.
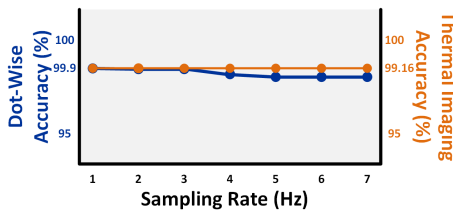

Figure 15: Both ThermoDot and ThermoNet's accuracy performance at sampling rates from one Hz to seven Hz.

9.5 Permanence Analysis

To investigate the permanence of ThermoWave, we collected multiple sessions of dot-wise temperature data on a single ThermoTag across three week. On the first week, approximately ten samples of data (i.e., temperature value ranged 35°F to 80°F with 0.1°F resolution) is collected each day to train a ThermoDot model. On the next two weeks, two samples of untrained data is collected each day
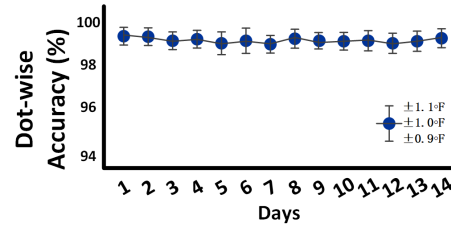

Figure 16: Plot of accuracy against time in days into permanence experiment across two weeks of testing period.

for testing the pre-trained ThermoDot model, and the predicted temperature vs. ground truth temperature is used to measure the accuracy. As shown in Fig. 16, ThermoDot model delivered over 99% of prediction is within the ±1.0°F precision, proving the ability to sustain a long period with high accuracy.

9.6 Environmental Dynamics

To determine whether ThermoWave can function under different environmental interferences such as humidity and vibration, a ThermoTag's thermal imaging performance is tested in simulated conditions. For the humidity simulation, a humidifier is placed in front of the cabinet and air at near dew point is blown into the cabinet to ensure ThermoTag is surrounded with humid air. For the vibration simulation, an actuator is placed on top of the cabinet vibrating consistently to introduce pseudo random vibration to the ThermoTag. Result in Fig. 17 proves that ThermoWave can maintain high accuracy while under humid and shaking conditions.
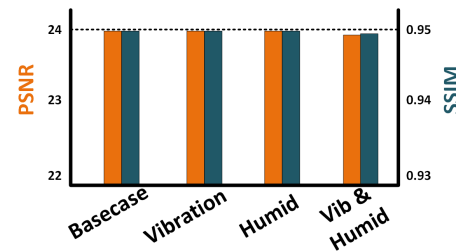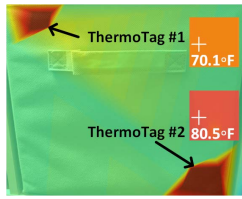

Figure 17: ThermoWave thermal imaging performance under environment interferences.

10 REAL WORLD TEST

To ensure that ThermoWave system remains accurate temperature sensing performance when it leaves lab condition, thus, we deploy ThermoWave in a complex scenario where multiple tags exist in a compact and NLOS setting with environmental disturbances. To determine ThermoWave's capability of recognizing multiple ThermoTags in a complex scenario, we attach two ThermoTags to the back of a storage box that is 20 cm away from each other (i.e., on the upper left corner and on the lower right corner of the box) for sensing. Next, to determine its resistance toward environment dynamics such as vibration and humidity, arbitrary water vapor in heated air is blown into the box while an actuator is generating arbitrary vibration inside the box. As shown in Fig. 18 and 19, ThermoWave is capable of identifying the positions of each ThermoTag and accurately reading thermal images. The confusion matrix

Figure 18: Two ThermoTags in the shelf box for thermal imaging.

Figure 19: Dot-wise temperature performance for the two ThermoTags in the box.

consists dot-wise temperature prediction accuracy for both of the ThermoTags. The average accuracy is determined to be 97.7% with ±1.0°F precision. In conclusion, ThermoWave system is capable of accurately recognizing ThermoTags position as well as inferring each of their temperature for both dot-wise and thermal imaging.

11 DISCUSSION AND LIMITATIONS

ThermoNet modeling: It is ideal to have a model that specifies which segment of thermal scattering response corresponds to a specific pixel in the resulting thermal image. Thus, it is appealing to utilize ThermoDot's model and expand feature extraction upon multiple frequencies to a dimension that matches the number of pixels in the ground truth. However, this technique is hindered by the computational overload and mmWave beam-forming precision which is too costly and too blurred at long distance, real-time sensing. Thus, current data-driven GAN methodology is applied.

Potential Medical Applications: ThermoTag's cholesteryl material is a common steroid chemical in mammalian organism's body [53, 54], meaning it is not inherently toxic and is often researched on medical domain. Beyond the experimentation of this paper, it is foreseeable that ThermoTag will be applied on human body for medical purposes, and possibly in human body for fine grained temperature monitoring. In addition, ThermoScanner's electromagnetic radiation is powered at 1.2 W with 8dBm radio transmission power at the range of two meters, which is insignificant when compared to modern wireless communication infrastructure, such as Wi-Fi. Moreover, the power can be further reduced in surgical application scenarios where the sensor is placed closer to the body. Thus, ThermoWave is a safe and ecological technology for medical applications in the near future.

Aging effect of film: It is common that material in the shape of film experience degradation(i.e., aging from wear, tear, or erosion). Preserving the shape of the sensor is also an important task in protecting the system. We came up with two solutions to protect ThermoWave film from the aging effect. **(i)** Cover the film with a protective material such as a thin sheet of PVC which is tested in our evaluation experiments that have little effect on the overall ThermoWave system's overall sensing ability. **(ii)** Design a calibration protocol such that accuracy is tested periodically. Once the accuracy falls below a threshold, replace the ThermoTag.

Metallic Occlusion: It is worth to mention that metallic objects are excellent at reflecting radio frequency waves, making wireless communication difficult with metallic occlusion. Consequently, when a sheet of metal lays in between ThermoTag and ThermoScanner, the thermal scattering response is unlikely to be generated considering the blockage.
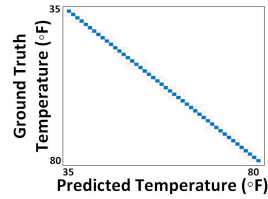
12 RELATED WORK

Wireless Temperature Monitoring: Existing wireless temperature monitoring technology can be placed into two categories based on their output (i.e., dot-wise temperature, and thermal image). The core of dot-wise temperature sensing systems [12, 55–59] is the thermal-electric sensor that delivers a temperature value. Such solution associates with high cost (i.e., a single passive RFID temperature tag is at least $1.00) and harms environment with heavy metal in its circuity. Moreover, wireless temperature senor such as the RFID tags are usually one-time use and create unsalvageable electronic waste [60]. On the other hand, thermal imaging devices reads temperature matrices by measuring the amplitude of electromagnetic wave in front of the imaging sensor, which fails if there is occlusion such as a piece of paper (e.g., infrared[13], mmWave[14]). Up to date, no wireless temperature monitoring technology is capable of ultra-low cost and ecological temperature sensing, as well as thermal imaging with occlusion.

mmWave Sensing: mmWave sensing has been growing popularity in different fields (e.g., 5G in telecommunication, object detection in autonomous driving, etc) in recent years. Many focus on macro motion and three-dimensional geometry of target object such as electronic identification, human gesture recognition, heart motion sensing, and tag pattern identification [61–68], while others focus on micro-motion and internal characteristic such as liquid classification and liquid crystal phase recognition [69–71]. To this date, ThermoWave is the first mmWave sensing system to perform ultra-low cost, ecological, and flexible temperature sensing using thermal scattering effect that achieves thermal imaging.

13 CONCLUSION

In this paper, we develop a novel mmWave technology-based paradigm, ThermoWave, for wireless temperature monitoring. The ThermoWave design exploits the thermal scattering effect, i.e., the changing ambient temperature can impact the scattering characteristics of the cholesteryl material when it is probed by RF signals. We fabricate a film-based temperature tag (i.e., ThermoTag) using cholesteryl material, which is attached on the target object. Then, we prototype a mmWave based ThermoScanner for interrogating thermal scattering response from ThermoTag. Finally, the response signals are fed to ThermoDot and ThermoNet model for dot-wise temperature recognition and thermal imaging, respectively. ThermoWave is capable of achieving the precision of ±1.0°F in the range of 30°F to 120°F for dot-wise temperature and ±3.0°F precision in thermal imaging. ThermoWave is promising to enable wireless signals to sense environmental and object temperature without the infrastructure support. Various experiments also proved robustness of ThermoWave, proving its potential to serve as the next generation temperature sensing technology.

ACKNOWLEDGMENTS

REFERENCES

[1] "Temperature-sensitive foods: focus on packaging." [Online]. Available: https://www.ups.com/us/es/services/knowledge-center/article.page?kid=a0e0087b

[2] M. Shomon, "Variations in temperature may be hazardous to your drugs," Jun 2019. [Online]. Available: https://www.verywellhealth.com/how-temperature-can-affect-medication-stability-3233264

[3] R. H. Bishara, "Cold chain management–an essential component of the global pharmaceutical supply chain," *American Pharmaceutical Review*, vol. 9, no. 1, pp. 105–109, 2006.

[4] S. James and C. James, "The food cold-chain and climate change," *Food Research International*, vol. 43, no. 7, pp. 1944–1956, 2010.

[5] "Temperature monitoring systems market." [Online]. Available: https://www.marketsandmarkets.com/Market-Reports/temperature-monitoring-system-market-250125379.html

[6] [Online]. Available: https://www.mordorintelligence.com/industry-reports/temperature-sensors-market-industry

[7] E. Shaulova and L. Biagi, "Smart home report 2019 - energy management." [Online]. Available: https://www.statista.com/study/36297/smart-home-report-energy-management/

[8] "Temperature sensor market." [Online]. Available: https://www.marketsandmarkets.com/Market-Reports/temperature-sensor-market-522.html

[9] R. Badia-Melis, U. Mc Carthy, L. Ruiz-Garcia, J. Garcia-Hierro, and J. R. Villalba, "New trends in cold chain monitoring applications-a review," *Food Control*, vol. 86, pp. 170–182, 2018.

[10] G. R. Mendez, M. A. M. Yunus, and S. C. Mukhopadhyay, "A wifi based smart wireless sensor network for monitoring an agricultural environment," in *2012 IEEE International Instrumentation and Measurement Technology Conference Proceedings*. IEEE, 2012, pp. 2640–2645.

[11] N. Sriskanthan, F. Tan, and A. Karande, "Bluetooth based home automation system," *Microprocessors and microsystems*, vol. 26, no. 6, pp. 281–289, 2002.

[12] A. Vaz, A. Ubarretxena, I. Zalbide, D. Pardo, H. Solar, A. Garcia-Alonso, and R. Berenguer, "Full passive uhf tag with a temperature sensor suitable for human body temperature monitoring," *IEEE Transactions on Circuits and Systems II: Express Briefs*, vol. 57, no. 2, pp. 95–99, 2010.

[13] J. M. Lloyd, *Thermal imaging systems*. Springer Science & Business Media, 2013.

[14] K. Mizuno, Y. Wagatsuma, H. Warashina, K. Sawaya, H. Sato, S. Miyanaga, and Y. Yamanaka, "Millimeter-wave imaging technologies and their applications," in *2007 IEEE International Vacuum Electronics Conference*. IEEE, 2007, pp. 1–2.

[15] S. Hocine, A. Brûlet, L. Jia, J. Yang, A. Di Cicco, L. Bouteiller, and M.-H. Li, "Structural changes in liquid crystal polymer vesicles induced by temperature variation and magnetic fields," *Soft Matter*, vol. 7, no. 6, pp. 2613–2623, 2011.

[16] D. Kondepudi and I. Prigogine, *Modern thermodynamics: from heat engines to dissipative structures*. John Wiley & Sons, 2014.

[17] J. L. Fergason, "Liquid crystals in nondestructive testing," *Applied Optics*, vol. 7, no. 9, pp. 1729–1737, 1968.

[18] "Digitimes research: 79ghz to replace 24ghz for automotive millimeter-wave radar sensors." [Online]. Available: www.digitimes.com/news/a20170906PD208.html

[19] "Single-chip 76-ghz to 81-ghz automotive radar sensor integrating dsp and mcu."

[20] "Cholesteryl benzoate." [Online]. Available: https://pubchem.ncbi.nlm.nih.gov/compound/Cholesteryl-benzoate

[21] T. Itahara, S. Furukawa, K. Kubota, M. Morimoto, and M. Sunose, "Cholesteryl benzoate derivatives: synthesis, transition property and cholesteric liquid crystal glass," *Liquid Crystals*, vol. 40, no. 5, pp. 589–598, 2013.

[22] C. E. Wilkes, J. W. Summers, C. A. Daniels, and M. T. Berard, *PVC handbook*. Hanser Munich, 2005, vol. 184.

[23] T. Kurashima, T. Horiguchi, and M. Tateda, "Distributed-temperature sensing using stimulated brillouin scattering in optical silica fibers," *Optics letters*, vol. 15, no. 18, pp. 1038–1040, 1990.

[24] M. V. Murhekar, S. Dutta, A. N. Kapoor, S. Bitragunta, R. Dodum, P. Ghosh, K. K. Swamy, K. Mukhopadhyay, S. Ningombam, K. Parmar *et al.*, "Frequent exposure to suboptimal temperatures in vaccine cold-chain system in india: results of temperature monitoring in 10 states," *Bulletin of the World Health Organization*, vol. 91, pp. 906–913, 2013.

[25] G. Schimetta, F. Dollinger, G. Scholl, and R. Weigel, "Wireless pressure and temperature measurement using a saw hybrid sensor," in *2000 IEEE Ultrasonics Symposium. Proceedings. An International Symposium (Cat. No. 00CH37121)*, vol. 1. IEEE, 2000, pp. 445–448.

[26] "Uhf 915 mhz temperature sensing rfid tags." [Online]. Available: https://www.rfidinc.com/uhf-915-mhz-temperature-sensing-rfid-tags

[27] Llc, "Mood sheet." [Online]. Available: https://www.sciplus.com/liquid-crystal-temperature-sheet-3676-p?gclid=Cj0KCQiA-bjyBRCcARIsAFboWg06AulONiTLgtAQ4W5NnScAEbA1GCn9utXG8gU5lsMaOrMC2UB9q1QaAjTeEALw_wcB

[28] Crow, "Polymer properties database." [Online]. Available: http://polymerdatabase.com/polymer%20physics/Excluded%20Volume2.html

[29] T. Wan, T. Zou, S.-X. Cheng, and R.-X. Zhuo, "Synthesis and characterization of biodegradable cholesteryl end-capped polycarbonates," *Biomacromolecules*, vol. 6, no. 1, pp. 524–529, 2005.

[30] J. Gilles, "Empirical wavelet transform," *IEEE transactions on signal processing*, vol. 61, no. 16, pp. 3999–4010, 2013.

[31] *Crest factor*. https://en.wikipedia.org/wiki/Crest_factor, Accessed: 2019-2-16.

[32] B. L'Huillier and A. Shafieloo, "Model-independent test of the flrw metric, the flatness of the universe, and non-local estimation of h0 rd," *Journal of Cosmology and Astroparticle Physics*, vol. 2017, no. 01, p. 015, 2017.

[33] K. V. Mardia, "Measures of multivariate skewness and kurtosis with applications," *Biometrika*, vol. 57, no. 3, pp. 519–530, 1970.

[34] R. I. Davis, W. Qiu, N. J. Heyer, Y. Zhao, M. Q. Yang, N. Li, L. Tao, L. Zhu, L. Zeng, D. Yao *et al.*, "The use of the kurtosis metric in the evaluation of occupational hearing loss in workers in china: Implications for hearing risk assessment," *Noise and Health*, vol. 14, no. 61, p. 330, 2012.

[35] B. Logan *et al.*, "Mel frequency cepstral coefficients for music modeling." in *ISMIR*, vol. 270, 2000, pp. 1–11.

[36] M. Sahidullah and G. Saha, "Design, analysis and experimental evaluation of block based transformation in mfcc computation for speaker recognition," *Speech Communication*, vol. 54, no. 4, pp. 543–565, 2012.

[37] Z. Qawaqneh, A. A. Mallouh, and B. D. Barkana, "Deep neural network framework and transformed mfccs for speaker's age and gender classification," *Knowledge-Based Systems*, vol. 115, pp. 5–14, 2017.

[38] F. Zheng, G. Zhang, and Z. Song, "Comparison of different implementations of mfcc," *Journal of Computer science and Technology*, vol. 16, no. 6, pp. 582–589, 2001.

[39] L. Muda, M. Begam, and I. Elamvazuthi, "Voice recognition algorithms using mel frequency cepstral coefficient (mfcc) and dynamic time warping (dtw) techniques," *arXiv preprint arXiv:1003.4083*, 2010.

[40] C. Kim and R. M. Stern, "Power-normalized cepstral coefficients (pncc) for robust speech recognition," *IEEE/ACM Transactions on Audio, Speech and Language Processing (TASLP)*, vol. 24, no. 7, pp. 1315–1329, 2016.

[41] M. T. Al-Kaltakchi, W. L. Woo, S. S. Dlay, and J. A. Chambers, "Study of fusion strategies and exploiting the combination of mfcc and pncc features for robust biometric speaker identification," in *2016 4th international conference on biometrics and forensics (IWBF)*. IEEE, 2016, pp. 1–6.

[42] M. Tamazin, A. Gouda, and M. Khedr, "Enhanced automatic speech recognition system based on enhancing power-normalized cepstral coefficients," *Applied Sciences*, vol. 9, no. 10, p. 2166, 2019.

[43] A. Liaw, M. Wiener *et al.*, "Classification and regression by randomforest," *R news*, vol. 2, no. 3, pp. 18–22, 2002.

[44] R. N. Bracewell and R. N. Bracewell, *The Fourier transform and its applications*. McGraw-Hill New York, 1986, vol. 31999.

[45] P. Isola, J.-Y. Zhu, T. Zhou, and A. A. Efros, "Image-to-image translation with conditional adversarial networks," in *Proceedings of the IEEE conference on computer vision and pattern recognition*, 2017, pp. 1125–1134.

[46] I. Goodfellow, J. Pouget-Abadie, M. Mirza, B. Xu, D. Warde-Farley, S. Ozair, A. Courville, and Y. Bengio, "Generative adversarial nets," in *Advances in neural information processing systems*, 2014, pp. 2672–2680.

[47] B. Xu, N. Wang, T. Chen, and M. Li, "Empirical evaluation of rectified activations in convolutional network," *arXiv preprint arXiv:1505.00853*, 2015.

[48] "Mlx90614 temperature sensor." [Online]. Available: https://www.sparkfun.com/datasheets/Sensors/Temperature/MLX90614_rev001.pdf

[49] "Flir one pro." [Online]. Available: https://www.flir.com/products/flir-one-pro/

[50] I. Lawrence and K. Lin, "A concordance correlation coefficient to evaluate reproducibility," *Biometrics*, pp. 255–268, 1989.

[51] Z. Wang, A. C. Bovik, H. R. Sheikh, E. P. Simoncelli *et al.*, "Image quality assessment: from error visibility to structural similarity," *IEEE transactions on image processing*, vol. 13, no. 4, pp. 600–612, 2004.

[52] Z. Wang, E. P. Simoncelli, and A. C. Bovik, "Multiscale structural similarity for image quality assessment," in *The Thrity-Seventh Asilomar Conference on Signals, Systems & Computers, 2003*, vol. 2. Ieee, 2003, pp. 1398–1402.

[53] S.-Y. Lin, C.-J. Ho, and M.-J. Li, "Precision and reproducibility of temperature response of a thermo-responsive membrane embedded by binary liquid crystals for drug delivery," *Journal of controlled release*, vol. 73, no. 2-3, pp. 293–301, 2001.

[54] J. W. Morzycki and A. Sobkowiak, "Electrochemical oxidation of cholesterol," *Beilstein journal of organic chemistry*, vol. 11, no. 1, pp. 392–402, 2015.

[55] D. Yeager, F. Zhang, A. Zarrasvand, and B. P. Otis, "A 9.2 μa gen 2 compatible uhf rfid sensing tag with- 12dbm sensitivity and 1.25 μvrms input-referred noise floor," in *2010 IEEE International Solid-State Circuits Conference-(ISSCC)*. IEEE, 2010, pp. 52–53.

[56] K. Opasjumruskit, T. Thanthipwan, O. Sathusen, P. Sirinamarattana, P. Gadmanee, E. Pootarapan, N. Wongkomet, A. Thanachayanont, and M. Thamsirianunt, "Self-powered wireless temperature sensors exploit rfid technology," *IEEE Pervasive computing*, vol. 5, no. 1, pp. 54–61, 2006.

[57] J. Yin, J. Yi, M. K. Law, Y. Ling, M. C. Lee, K. P. Ng, B. Gao, H. C. Luong, A. Bermak, M. Chan *et al.*, "A system-on-chip epc gen-2 passive uhf rfid tag with embedded temperature sensor," *IEEE Journal of Solid-State Circuits*, vol. 45, no. 11, pp. 2404–2420, 2010.

[58] Y. Wang, Y. Jia, Q. Chen, and Y. Wang, "A passive wireless temperature sensor for harsh environment applications," *Sensors*, vol. 8, no. 12, pp. 7982–7995, 2008.

[59] R. Kuchta and R. Vrba, "Wireless temperature sensor system," in *International Conference on Networking, International Conference on Systems and International Conference on Mobile Communications and Learning Technologies (ICNICON-SMCL'06)*, April 2006, pp. 163–163.

[60] S. Daniel and S. Tadatomo, "Perspectives for the application of rfid on electric and electronic waste," in *Advances in Life Cycle Engineering for Sustainable Manufacturing Businesses*. Springer, 2007, pp. 359–364.

[61] Z. Li, Z. Yang, C. Song, C. Li, Z. Peng, and W. Xu, "E-eye: Hidden electronics recognition through mmwave nonlinear effects," in *Proceedings of the 16th ACM Conference on Embedded Networked Sensor Systems*. ACM, 2018, pp. 68–81.

[62] Y. Zhu, Y. Zhu, Z. Zhang, B. Y. Zhao, and H. Zheng, "60ghz mobile imaging radar," in *Proceedings of the 16th International Workshop on Mobile Computing Systems and Applications*. ACM, 2015, pp. 75–80.

[63] J. Lien, N. Gillian, M. E. Karagozler, P. Amihood, C. Schwesig, E. Olson, H. Raja, and I. Poupyrev, "Soli: Ubiquitous gesture sensing with millimeter wave radar," *ACM Transactions on Graphics (TOG)*, vol. 35, no. 4, p. 142, 2016.

[64] F. Lin, C. Song, Y. Zhuang, W. Xu, C. Li, and K. Ren, "Cardiac scan: A non-contact and continuous heart-based user authentication system," in *Proceedings of the 23rd Annual International Conference on Mobile Computing and Networking*. ACM, 2017, pp. 315–328.

[65] F. Lin, Y. Zhuang, C. Song, A. Wang, Y. Li, C. Gu, C. Li, and W. Xu, "Sleepsense: A noncontact and cost-effective sleep monitoring system," *IEEE transactions on biomedical circuits and systems*, vol. 11, no. 1, pp. 189–202, 2016.

[66] T. Wei and X. Zhang, "mtrack: High-precision passive tracking using millimeter wave radios," in *Proceedings of the 21st Annual International Conference on Mobile Computing and Networking*. ACM, 2015, pp. 117–129.

[67] Z. Li, B. Chen, Z. Yang, H. Li, C. Xu, X. Chen, K. Wang, and W. Xu, "Ferrotag: A paper-based mmwave-scannable tagging infrastructure," in *To appear in Proceedings of the 17th ACM Conference on Embedded Networked Sensor Systems*, ser. SenSys'19, 2019.

[68] C. Xu, Z. Li, H. Zhang, A. S. Rathore, H. Li, C. Song, K. Wang, and W. Xu, "Waveear: Exploring a mmwave-based noise-resistant speech sensing for voice-user interface," in *Proceedings of the 17th Annual International Conference on Mobile Systems, Applications, and Services*, 2019, pp. 14–26.

[69] T. Ozturk, "Characterization of liquids using electrical properties in microwave and millimeter wave frequency bands," *Journal of Nondestructive Evaluation*, vol. 38, no. 1, p. 11, 2019.

[70] ——, "Classification of measured unsafe liquids using microwave spectroscopy system by multivariate data analysis techniques," *Journal of hazardous materials*, vol. 363, pp. 309–315, 2019.

[71] Z. Li, F. Ma, A. S. Rathore, Z. Yang, B. Chen, L. Su, and W. Xu, "Wavespy: Remote and through-wall screen attack via mmwave sensing," in *To appear in IEEE Symposium on Security and Privacy 2020*, ser. S&P'20, 2020.